Analysis and Experimental Verification of Radial-Gap Two-Degree-of-Freedom Motor Based on a Magnetic Screw Structure

Yoshiyuki Hatta, *Member, IEEE*, Yasutaka Fujimoto, *Senior Member, IEEE*, Tomoyuki Shimono, *Senior Member, IEEE*, and Kazuaki Ito, *Senior Member, IEEE*

***Abstract*—This article proposes a radial-gap two-degree-of-freedom motor based on a magnetic screw structure. The proposed motor is composed of stator parts, rotor parts, and a mover part, and can generate torque and thrust force simultaneously and independently. Additionally, the motor can generate a large thrust force with the magnetic screw structure. In the proposed motor, the rotor parts and mover part, which act as the nut and screw of ball screws, are coupled with each other by means of magnetic force. Therefore, there is no friction between the rotor parts and mover part. The proposed motor can not only contribute to the minimization of multidegree-of-freedom systems, such as industrial robots but also improve the energy efficiency of robots. This article examines the effectiveness of the proposed motor through analysis and experimental results.**

***Index Terms*—2-degrees-of-freedom (DOF) motor, magnet screw, magnetic gear, multi-DOF, radial-gap machine.**

I. Introduction

In GENERAL, industrial robots have a multidegree-of-freedom (multi-DOF) structure so that they can perform human tasks, and more DOFs are necessary as the robots perform more complex tasks. However, one DOF generally consists of one motor so that each DOF can be controlled independently. As a result, robots become larger and heavier as more complex tasks are necessary.

The increase in the number of motors signifies an increased number of parts that require maintenance. Any parts have their life spans and will be broken sometime. They need maintenance, such as part replacement when they are broken or before. Therefore, the increase in parts including motors, connectors between the motors and other parts, bolts to fix the connectors, and so on lead to the increase in the number of parts that need maintenance.

Manuscript received 4 October 2021; revised 8 December 2021 and 4 March 2022; accepted 5 April 2022. Date of publication 6 May 2022; date of current version 14 December 2022. Recommended by Technical Editor P. Yan. *(Corresponding author: Yoshiyuki Hatta.)*

Yoshiyuki Hatta and Kazuaki Ito are with Gifu University, Gifu 501-1193, Japan (e-mail: y_hatta@gifu-u.ac.jp; kazu_it@gifu-u.ac.jp).

Yasutaka Fujimoto and Tomoyuki Shimono are with Yokohama National University, Yokohama 240-8501, Japan (e-mail: fujimoto@ynu.ac.jp; shimono@ynu.ac.jp).

Color versions of one or more figures in this article are available at https://doi.org/10.1109/TMECH.2022.3168144.

Digital Object Identifier 10.1109/TMECH.2022.3168144

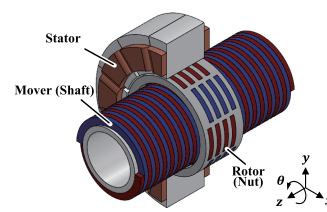

Fig. 1. Radial-gap helical ROTLIN machine [21] (the conventional motor).

Moreover, the number of robots, which are composed of many parts, is increasing in the industrial field. However, many kinds of maintenance are done by humans. The increase in robots causes an increase in manpower to maintain them, although the number of workers is expected to decrease in the future. Research on multi-DOF motors has attracted attention because these motors can reduce the total number of motors in robots, while retaining the number of DOFs.

One type of multi-DOF motor is a spherical motor [1]–[3], which is composed of a spherical mover and a stator that covers the mover. This motor has two or three DOFs, and its mover rotates around multiple axes. Additionally, multi-DOF motors that perform not only rotational motion but also linear motion have been proposed [4]–[11]. Actuators which realize 2-D or 3-D motion with piezoelectric elements have been proposed [12]–[14].

Although the solution of size and weight are required of the industrial robots, the improvement of energy efficiency is also required. Each joint of industrial robots is composed of a motor and a gear so that the robots can generate a large force; however, gears generally cause energy loss. Therefore, it is important to improve not only the motors but also the power transmission, including the gears, to increase the energy efficiency of the robots.

Recently, to reduce power transmission loss, research on magnetic gears has been conducted [15]–[17]. In a magnetic gear, the input part is coupled to the output part by means of magnetic force. There is no friction between the input part and output part because they are connected without physical contact. Therefore, magnetic gears can reduce transmission loss [18].

Not only magnetic gears but also magnetic screws have been researched [19], [20]. Additionally, the radial-gap helical ROTLIN motor, which is a combination of a rotary motor and a magnetic screw, as shown in Fig. 1, has been proposed [21]. A

TABLE I
COMPONENTS INCLUDED IN EACH PART OF RADIAL-GAP ROTLIN MACHINE AND RADIAL-GAP 2-DOF MOTOR

Parts of motors		Components			
		Rotary motor for right-hand magnetic screw	Right-hand magnetic screw	Rotary motor for left-hand magnetic screw	Left-hand magnetic screw
Radial-gap ROTLIN Machine	Stator	Stator	-	-	-
	Rotor	Rotor	Nut part	-	-
	Mover	-	Screw part	-	-
Radial-Gap 2-DOF Motor	R-stator part	Stator	-	-	-
	R-rotor part	Rotor [Fig. 4 (a)]	Nut part [Fig. 4 (b)]	-	-
	L-stator part	-	-	Stator	-
	L-rotor part	-	-	Rotor [Fig. 5 (a)]	Nut part [Fig. 5 (b)]
	Mover part	-	Screw part [Fig. 6 (a)]	-	Screw part [Fig. 6 (b)]
Characteristics of components		Screw part outputs the left-helical force depending on the rotation of nut part rotated by rotary motor		Screw part outputs the right-helical force depending on the rotation of nut part rotated by rotary motor	

magnetic screw has the structure of a ball screw and is composed of a screw part and nut part, which have spiral permanent magnets (PMs). They are coupled to each other by means of magnetic force. The helical force around the central axis of the screw part is generated in the screw part by the rotation of the nut part. By canceling the rotation of the screw part, the only linear component in the helical force is the output of the screw part. Therefore, a magnetic screw can convert rotational motion into linear motion. The reduction ratio of the rotational velocity to the linear velocity can be adjusted by the lead length of the magnetic screw. The magnetic screw can generate a large thrust force by shortening the lead length.

As mentioned above, a multi-DOF motor is an important element for addressing the decreasing birthrate and aging of the population. Therefore, the development of multi-DOF motors that generate a large force with low transmission loss can make a significant contribution to the industrial field. The authors thus propose a radial-gap two-degree-of-freedom (2-DOF) motor based on a magnetic screw structure [22].

The proposed motor is composed of two stator parts, two rotor parts, and a mover part. It can remove parts that a conventional 2-DOF device with a rotary motor and a linear actuator needs. The proposed motor does not have a connector that the conventional device needs between the rotary motor and the linear actuator. Additionally, it integrates several parts required for the linear actuator, composed of a rotary motor and a ball screw. The rotor part in the proposed motor combines the rotor of the rotary motor, the input part of the ball screw, and the coupling between them. Moreover, the proposed motor can generate a large thrust force because it has a magnetic screw structure. The authors evaluate the effectiveness of the proposed motor using finite element analysis (FEA).

This article also establishes a mathematical representation of the proposed radial-gap 2-DOF motor. Additionally, the effectiveness of the proposed motor is evaluated based on both analysis results and experimental results.

II. PRINCIPLE OF PROPOSED RADIAL-GAP TWO-DEGREE-OF-FREEDOM MOTOR

A. Structure of Proposed Motor

Table I shows the summary of components in the proposed motor illustrated in Fig. 2 and the ROTLIN machine [21].

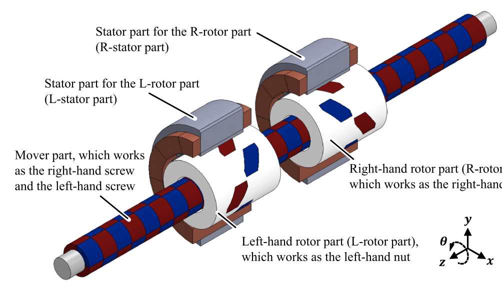

Fig. 2. Radial-gap 2-DOF motor (the proposed motor).

TABLE II
DESIGN PARAMETERS OF RADIAL-GAP TWO-DEGREE-OF-FREEDOM MOTOR

Radius of shaft [mm]	r_{sh}	6.00
Radius of mover part [mm]	r_M	9.00
Inner radius of rotor parts [mm]	r_{Rin}	9.80
Outer radius of rotor part [mm]	r_{Rout}	18.8
Length of air gap between rotor and stator parts [mm]	l_g	0.80
Radius of stator part [mm]	r_S	35.0
Stack length of stator part [mm]	l_S	30.0
Distance between stator parts [mm]	l_d	45.0
Length of mover part [mm]	l_M	280
Pitch or lead length of screw [mm]	l_p	40.0
Number of turns of windings		160
Material of permanent magnets in mover part		N42
Material of permanent magnets in rotor parts		N40SH
Residual magnetic flux density of N40SH [T]	B_r	1.29
Magnetic permeability of neodymium magnet [H/m]	μ_m	1.32×10^{-6}
Material of shaft		SS400
Material of cores in the stator		15HX1000

Table II presents the design parameters including the ones shown in Fig. 3. The ROTLIN machine comprises a stator, a rotor, and a mover that moves only in the z-direction. The structure integrates some components, including a rotary motor and a right-hand magnetic screw, into the ROTLIN machine. The rotation of the nut part, which is included in the rotor, as shown in Table I, generates a left-helical force in the mover. The mover moves in the z-direction by the left-helical force.

On the other hand, the proposed motor is composed of two stator parts, two rotor parts, and a mover part that moves in

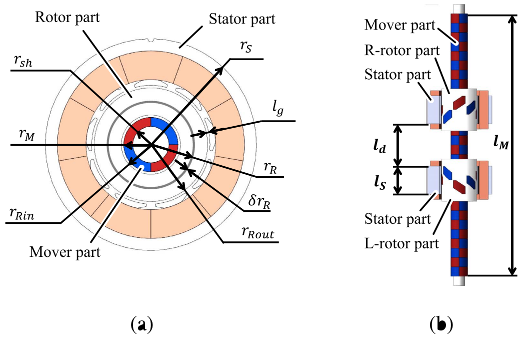

Fig. 3. (a) Front view and (b) top view of motor.

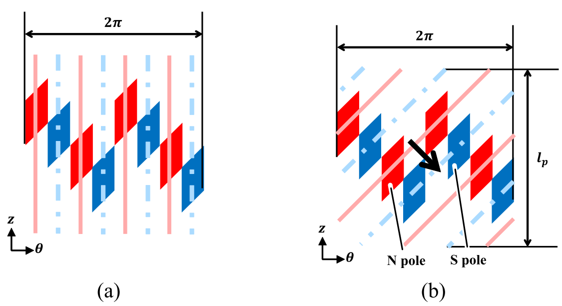

Fig. 4. Arrangement of permanent magnets in R-rotor part. (a) Components for a rotary motor. (b) Components for a nut part.

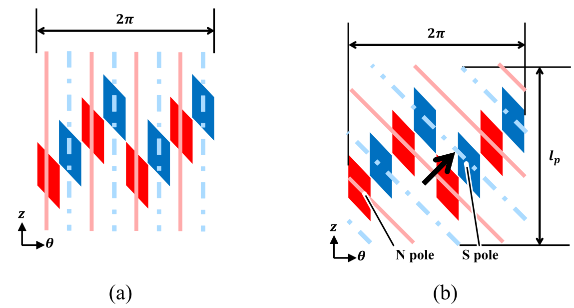

Fig. 5. Arrangement of permanent magnets in the L-rotor part. (a) Components for a rotary motor. (b) Components for a nut part.

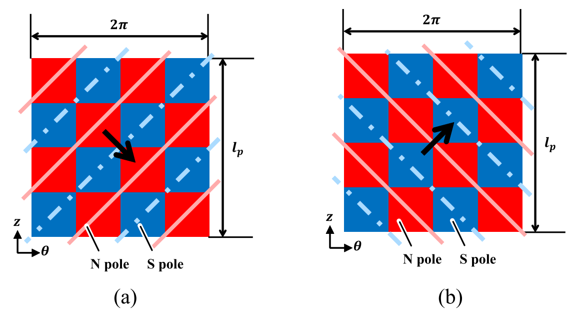

Fig. 6. Arrangement of permanent magnets in the mover part. (a) Right-hand components. (b) Left-hand components.

the θ direction and the z-direction. Some parts have the special arrangements of PMs to integrate rotary motors, a right-hand magnetic screw, and a left-hand magnetic screw into the proposed motor. The PM arrangement in rotor parts works as a rotor in the rotary motor and the nut part, as shown in Table I. The mover part has the PM arrangement which realizes both a right-hand screw and a left-hand screw. Therefore, the mover part can output left-helical and right-helical forces.

Additionally, the left-helical and right-helical forces are generated independently in the mover part because each of the rotor parts rotates independently. Therefore, torque in the θ direction and thrust force in the z-direction are generated independently by the combination of two kinds of helical-direction forces. In the section, the principle to generate the torque and thrust force is described.

Fig. 4 displays the PM arrangement in the R-rotor part. The light-colored lines in Fig. 4(a) indicate the PM arrangement for a rotor of the rotary motor. The N and S poles of the PMs are arranged alternately along the θ direction and interact with the stator part. In the proposed motor, the stator parts and rotor parts are designed based on a nine-slot–eight-pole (9s8p) rotary motor, which contributes to the dispersion of radial forces and the decrease in noise and cogging torque. Therefore, four N poles and four S poles are arranged in the rotor parts.

Additionally, the PMs are formed so that the N and S poles are arranged alternately along the left helical direction, as the light-colored lines illustrated in Fig. 4(b). In the figure, l_p represents the lead length of the R-rotor part. The PM arrangement functions as the right-hand nut part with a double screw.

Fig. 5 displays the PM arrangement in the L-rotor part. The PM arrangement displayed by the light-colored lines in Fig. 5(a) constitutes the rotor in the rotary motor. Additionally, the PMs are formed so that the N and S poles are arranged alternately along the right helical direction, as the light-colored lines in Fig. 5(b). The arrangement functions as the left-hand nut part.

In the mover part, the PMs have a 2-D arrangement, and the N and S poles are arranged alternately along the left helical direction, as the light-colored lines illustrated in Fig. 6(a). Additionally, the N and S poles are arranged alternately along the right helical direction, as the light-colored lines in Fig. 6(b). The mover part functions as the right-hand and left-hand screw parts, as shown in Table I.

The phase of the light-colored lines between Figs. 4(b) and 6(a) changes, when the R-rotor part rotates or the mover part moves in the left helical direction. The phase generates a magnetic force in the left helical direction in the mover part. In contrast, the phase of the light-colored lines between Figs. 5(b) and 6(b) changes, when the L-rotor part rotates or the mover part moves in the right helical direction. The phase generates a magnetic force in the right helical direction. Therefore, the proposed motor can generate a torque in the θ direction and a thrust force in the z-direction independently by the combination of the magnetic force in two helical directions.

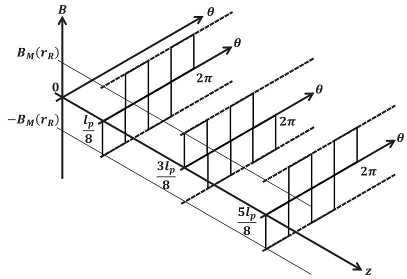

Fig. 7. Magnetic flux density generated by mover parts.

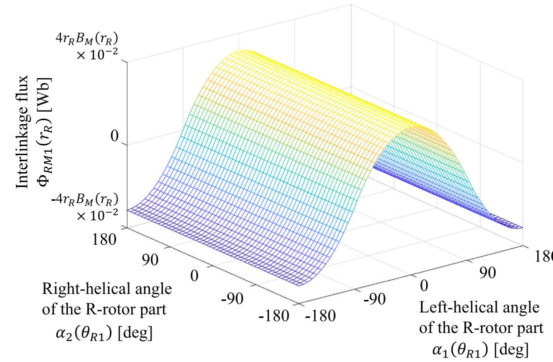

Fig. 8. Calculation results of the ratio of the interlinkage flux to the magnetic flux density.

B. Modeling the Relationship Between Rotor Parts and Mover Part

The proposed motor is a combination of rotary motors and magnetic screws. This subsection describes the magnetic screws, which are composed of rotor parts and a mover part.

First, it is assumed that rotor parts with a thickness of δr_R are placed at $r = r_R$, as illustrated in Fig. 3(a). The interlinkage flux interlinking with the R-rotor part is calculated as follows:

$$\Phi_{RM1}(r_R) = \Phi_{\mathrm{RNM1}} - \Phi_{\mathrm{RSM1}} \tag{1}$$

$$\Phi_{\mathrm{RNM1}} = \Phi_{M1}\left(\theta_{R1} - \theta_M - \frac{\pi}{4}, z_M\right) \tag{2}$$

$$\Phi_{\mathrm{RSM1}} = -\Phi_{M1}\left(\theta_{R1} - \theta_M - \pi, z_M + \frac{l_p}{8}\right) \tag{3}$$

where $\Phi_{RM1}(r_R)$ represents the interlinkage flux, which is generated by the mover part and interlinks with the PMs of the R-rotor part; θ_{R1} indicates the position of the R-rotor part in the θ direction; and θ_M and z_M denote the positions of the mover part in the θ and z-directions, respectively.

The magnetic flux density, which interlinks with the PMs of the R-rotor part, depends on r_R and is defined as in Fig. 7, where $B_M(r_R)$ represents the amplitude of the magnetic flux density at $r = r_R$. The interlinkage flux is defined with $B_M(r_R)$. Φ_{M1} is calculated as

$$\Phi_{M1}\left(\theta + \pi j, z + \frac{l_p}{2}k\right) = \begin{cases} -4B_M(r_R)\cdot S_1\left(\theta + \frac{\pi}{2}, z\right) & \text{if } -\frac{\pi}{2} \le \theta < -\frac{\pi}{4} \\ 4B_M(r_R)\cdot S_2(\theta, z) & \text{if } -\frac{\pi}{4} \le \theta < 0 \\ 4B_M(r_R)\cdot S_1(\theta, z) & \text{if } 0 \le \theta < \frac{\pi}{4} \\ -4B_M(r_R)\cdot S_2\left(\theta - \frac{\pi}{2}, z\right) & \text{if } \frac{\pi}{4} \le \theta < \frac{\pi}{2} \end{cases} \tag{4}$$

$$j = \cdots -2, -1, 0, 1, 2\cdots$$

$$-\frac{l_p}{4} \le z < \frac{l_p}{4}, \quad k = \cdots -2, -1, 0, 1, 2\cdots$$

$$S_1(\theta, z) = \begin{cases} -C_1\cdot\left(z^2 + \frac{1}{3}zl_p + \frac{3}{128}l_p^2\right) & \text{if } -\frac{l_p}{4} \le z < -\frac{l_p}{8} \\ -C_2\cdot\left(z + \frac{1}{16}l_p\right) & \text{if } -\frac{l_p}{8} \le z < 0 \\ C_1\cdot\left(z^2 - \frac{1}{8}zl_p + \frac{1}{128}l_p^2\right) & \text{if } 0 \le z < \frac{l_p}{8} \\ C_2\cdot\left(z - \frac{3}{16}l_p\right) & \text{if } \frac{l_p}{8} \le z < \frac{l_p}{4} \end{cases} \tag{5}$$

$$S_2(\theta, z) = \begin{cases} C_1\cdot\left(z^2 + \frac{8\theta+5\pi}{8\pi}zl_p + \frac{32\theta^2+48\pi\theta+13\pi^2}{128\pi^2}l_p^2\right) \\ \quad \text{if } -\frac{l_p}{4} \le z < -\frac{l_p}{8} \text{ and } z < -\frac{1}{2\pi}\left(\theta + \frac{\pi}{2}\right)l_p \\ -C_1\cdot\left(z^2 + \frac{8\theta+3\pi}{8\pi}zl_p + \frac{32\theta^2+16\pi\theta+3\pi^2}{128\pi^2}l_p^2\right) \\ \quad \text{if } -\frac{l_p}{4} \le z < -\frac{l_p}{8} \text{ and } -\frac{1}{2\pi}\left(\theta + \frac{\pi}{2}\right)l_p \le z \\ -4r_R\cdot\left(\frac{8\theta+\pi}{8}z + \frac{32\theta^2+16\pi\theta+\pi^2}{128}l_p\right) \\ \quad \text{if } -\frac{l_p}{8} \le z < 0 \\ -C_1\cdot\left(z^2 + \frac{8\theta+\pi}{8\pi}zl_p + \frac{32\theta^2+16\pi\theta+\pi^2}{128\pi^2}l_p^2\right) \\ \quad \text{if } 0 \le z < \frac{l_p}{8} \text{ and } z < -\frac{\theta}{2\pi}l_p \\ C_1\cdot\left(z^2 + \frac{8\theta-\pi}{8\pi}zl_p + \frac{32\theta^2-16\pi\theta-\pi^2}{128\pi^2}l_p^2\right) \\ \quad \text{if } 0 \le z < \frac{l_p}{8} \text{ and } -\frac{\theta}{2\pi}l_p \le z \\ 4r_R\cdot\left(\frac{8\theta+\pi}{8}z + \frac{32\theta^2-16\pi\theta-3\pi^2}{128}l_p\right) \\ \quad \text{if } \frac{l_p}{8} \le z < \frac{l_p}{4} \end{cases} \tag{6}$$

$$C_1 = \frac{4\pi r_R}{l_p} \tag{7}$$

$$C_2 = \frac{\pi r_R}{2}. \tag{8}$$

Fig. 8 displays $\Phi_{RM1}(r_R)$, which is calculated with (1)–(8) and Table II. In the figure, $\alpha_{1(\theta_{R1})}$ and $\alpha_2(\theta_{R1})$ are defined as follows:

$$\alpha_1(\theta_{R1}) = 2(\theta_{R1} - \theta_M) + \frac{4\pi}{l_p}z_M \tag{9}$$

$$\alpha_2(\theta_{R1}) = 2(\theta_{R1} - \theta_M) - \frac{4\pi}{l_p}z_m. \tag{10}$$

Here, $\alpha_1(\theta_{R1})$ denotes the motion of the R-rotor part toward the mover part in the left helical direction, while $\alpha_2(\theta_{R1})$ denotes the motion in the right helical direction. Fig. 8 indicates that $\Phi_{RM1}(r_R)$ is dependent on $\alpha_1(\theta_{R1})$ but independent of $\alpha_2(\theta_{R1})$. Additionally, the relationship between $\Phi_{RM1}(r_R)$ and $\alpha_1(\theta_{R1})$

is close to a cosine wave. Therefore, $\Phi_{RM1}(r_R)$ approaches the following:

$$\Phi_{RM1}(r_R) = \Phi_{aRM1}(r_R) \cdot \cos(\alpha_1(\theta_{R1})) \quad (11)$$

where $\Phi_{aRM1}(r_R)$ is a value depending on r_R.

The inductance matrix between the R-rotor part and mover part $\boldsymbol{L}_{RM1}(r_R)$ is described by

$$\boldsymbol{L}_{RM1}(r_R) = \begin{bmatrix} L_{R1} & M_{RM1} \\ M_{RM1} & L_M \end{bmatrix} \quad (12)$$

$$M_{RM1} = \frac{\Phi_{aRM1}(r_R) \cdot \cos(\alpha_1(\theta_{R1}))}{I_{mM}} \quad (13)$$

where L_{R1} and L_M represent the self-inductance of the R-rotor part and mover part, respectively, and I_{mM} indicates the equivalent magnetization current of the PMs in the mover part. Therefore, the torque and thrust force generated by the R-rotor part with a thickness of δr_R are calculated as follows:

$$\delta T_{M1} = \frac{1}{2}\begin{bmatrix} I_{mR} \\ I_{mM} \end{bmatrix}^T \frac{\partial \boldsymbol{L}_{RM1}(r_R)}{\partial \theta_M} \begin{bmatrix} I_{mR} \\ I_{mM} \end{bmatrix} \quad (14)$$

$$\delta F_{M1} = \frac{1}{2}\begin{bmatrix} I_{mR} \\ I_{mM} \end{bmatrix}^T \frac{\partial \boldsymbol{L}_{RM1}(r_R)}{\partial z_M} \begin{bmatrix} I_{mR} \\ I_{mM} \end{bmatrix}. \quad (15)$$

Here, δT_{M1} and δF_{M1} represent the torque and thrust force generated in the mover part, and I_{mR} is the equivalent magnetization current of the PMs in the rotor parts, which is defined as follows:

$$I_{mR} = \frac{B_r \cdot \delta r_R}{\mu_m} \quad (16)$$

where B_r and μ_m represent the residual magnetic flux density and magnetic permeability of the R-rotor part, respectively. The torque and thrust force generated by the entire PM in the R-rotor part are calculated as

$$T_{M1} = \int dT_{M1} = T_{aM1}\sin(\alpha_1(\theta_{R1})) \quad (17)$$

$$T_{aM1} = \int_{r_{\mathrm{Rin}}}^{r_{\mathrm{Rout}}} 2\frac{B_r}{\mu_m}\Phi_{aRM1}(r_R)\,dr_R \quad (18)$$

$$F_{M1} = \int dF_{M1} = -F_{aM1}\sin(\alpha_1(\theta_{R1})) \quad (19)$$

$$F_{aM1} = \int_{r_{\mathrm{Rin}}}^{r_{\mathrm{Rout}}} \frac{4\pi}{l_p}\frac{B_r}{\mu_m}\Phi_{aRM1}(r_R)\,dr_R. \quad (20)$$

The PM arrangements in the R-rotor and L-rotor parts are symmetric. The interlinkage flux interlinking with the L-rotor part $\Phi_{RM2}(r_R)$ is defined as

$$\Phi_{RM2}(r_R) = \Phi_{aRM2}(r_R) \cdot \cos(\alpha_2(\theta_{R2})) \quad (21)$$

where $\Phi_{aRM2}(r_R)$ is a value depending on r_R, like $\Phi_{aRM1}(r_R)$. The inductance matrix between the L-rotor part and mover part $\boldsymbol{L}_{RM2}(r_R)$ is described by

$$\boldsymbol{L}_{RM2}(r_R) = \begin{bmatrix} L_{R2} & M_{RM2} \\ M_{RM2} & L_M \end{bmatrix} \quad (22)$$

$$M_{RM2} = \frac{\Phi_{aRM2}(r_R) \cdot \cos(\alpha_2(\theta_{R2}))}{I_{mM}} \quad (23)$$

where L_{R2} represents the self-inductance of the L-rotor part. The torque and thrust force generated by the L-rotor part with a thickness of δr_R are calculated as follows:

$$\delta T_{M2} = \frac{1}{2}\begin{bmatrix} I_{mR} \\ I_{mM} \end{bmatrix}^T \frac{\partial \boldsymbol{L}_{RM2}(r_R)}{\partial \theta_M} \begin{bmatrix} I_{mR} \\ I_{mM} \end{bmatrix} \quad (24)$$

$$\delta F_{M2} = \frac{1}{2}\begin{bmatrix} I_{mR} \\ I_{mM} \end{bmatrix}^T \frac{\partial \boldsymbol{L}_{RM2}(r_R)}{\partial z_M} \begin{bmatrix} I_{mR} \\ I_{mM} \end{bmatrix}. \quad (25)$$

From these formulas, the torque and thrust force generated by the entire PM in the L-rotor part are calculated as

$$T_{M2} = \int dT_{M2} = T_{aM2}\sin(\alpha_2(\theta_{R2})) \quad (26)$$

$$T_{aM2} = \int_{r_{Rin}}^{r_{R\mathrm{out}}} 2\frac{B_r}{\mu_m}\Phi_{aRM2}(r_R)\,dr_R \quad (27)$$

$$F_{M2} = \int dF_{M2} = F_{aM2}\sin(\alpha_2(\theta_{R2})) \quad (28)$$

$$F_{aM2} = \int_{r_{Rin}}^{r_{R\mathrm{out}}} \frac{4\pi}{l_p}\frac{B_r}{\mu_m}\Phi_{aRM2}(r_R)\,dr_R. \quad (29)$$

In the proposed motor, the R-rotor and L-rotor parts have a symmetric structure. The amplitude of the interlinkage flux is defined as $\Phi_{aRM}(r_R) = \Phi_{aRMi}(r_R)\ (i \in 1, 2)$. In this article, suffixes 1 and 2 represent the components of the right-hand screw and left-hand screw, respectively. T_{Mi} and F_{Mi} are described as (30)–(33), respectively,

$$T_{Mi} = T_{aM}\sin(\alpha_i(\theta_{Ri})) \quad (30)$$

$$T_{aM} = \int_{r_{\mathrm{Rin}}}^{r_{\mathrm{Rout}}} 2\frac{B_r}{\mu_m}\Phi_{aRM}(r_R)\,dr_R \quad (31)$$

$$F_{Mi} = (-1)^i F_{aM}\sin(\alpha_i(\theta_{Ri})) \quad (32)$$

$$F_{aM} = \int_{r_{\mathrm{Rin}}}^{r_{\mathrm{Rout}}} \frac{4\pi}{l_p}\frac{B_r}{\mu_m}\Phi_{aRM}(r_R)\,dr_R. \quad (33)$$

The ratio of the thrust force to the torque is calculated as

$$G_r = \left|\frac{F_{Mi}}{T_{Mi}}\right| = \frac{2\pi}{l_p} \quad (34)$$

where G_r is equivalent to the ratio of general ball screws. It turns out that the proposed motor can convert the torque input to the rotor parts into a large thrust force by adjusting G_r. However, the maximum F_{Mi} is F_{aM}, as shown in (32) and (33). Because of that, it is necessary to consider not only G_r but also B_r and $\Phi_{aRM}(r_R)$, which F_{aM} depends on, to generate a large thrust force in the mover part.

C. Modeling the Relationship Between Rotor Parts and Stator Parts

This subsection describes the rotary motors, which are composed of rotor parts and stator parts. The stator parts are composed of three-phase coils and cores. Therefore, the voltage equation of each stator part is represented as follows:

$$\boldsymbol{V}_{Si} = [V_{uSi}, V_{vSi}, V_{wSi}, V_{mSi}]^T$$
$$= \boldsymbol{R}_{Si}\boldsymbol{I}_{Si} + \boldsymbol{L}_{SRi}\frac{d\boldsymbol{I}_{Si}}{dt} + \dot{\theta}_{Ri}\frac{\partial \boldsymbol{L}_{SRi}}{\partial \theta_{Ri}}\boldsymbol{I}_{Si} \tag{35}$$

$$\boldsymbol{I}_{Si} = [I_{uSi}, I_{vSi}, I_{wSi}, I_{mRi}]^T \tag{36}$$

$$\boldsymbol{R}_{Si} = \begin{bmatrix} R_{Si} & 0 & 0 & 0 \\ 0 & R_{Si} & 0 & 0 \\ 0 & 0 & R_{Si} & 0 \\ 0 & 0 & 0 & 0 \end{bmatrix} \tag{37}$$

$$\boldsymbol{L}_{SRi} = \begin{bmatrix} L_{Si} & -M_{Si} & -M_{Si} & M_{\Phi 1i} \\ -M_{Si} & L_{Si} & -M_{Si} & M_{\Phi 2i} \\ -M_{Si} & -M_{Si} & L_{Si} & M_{\Phi 3i} \\ M_{\Phi 1i} & M_{\Phi 2i} & M_{\Phi 3i} & K \end{bmatrix} \tag{38}$$

$$M_{\Phi ji} = \frac{\Phi_{aSRi}}{I_{mRi}} \cos\left(\theta'_{Ri} - \frac{2(j-1)}{3}\pi\right) \tag{39}$$

$$\theta'_{Ri} = 4\theta_{Ri} \tag{40}$$

where I_{uSi}, I_{vSi}, and I_{wSi} represent the current of each phase in the stator part, and I_{mRi} indicates the equivalent magnetization current of the PMs in the rotor part. Each component of $\boldsymbol{V}_{Si}$ is the voltage corresponding to I_{uSi}, I_{vSi}, I_{wSi}, and I_{mRi}. Furthermore, θ'_{Ri} is the electrical angle defined based on the period of the PM arrangement in the θ direction. In addition, $\Phi_{aSR} = \Phi_{aSRi}\,(i \in 1, 2)$ is the amplitude of the interlinkage flux, which is generated by the rotor part and interlinks with the stator part. The torque generated by the current of the stator part is calculated as

$$T_{Ri} = \frac{1}{2}\begin{bmatrix} I_{dSi} \\ I_{qSi} \\ I_{0Si} \\ I_{mRi} \end{bmatrix}^T \boldsymbol{C}\frac{\partial \boldsymbol{L}_{SRi}}{\partial \theta_{Ri}}\boldsymbol{C}^T \begin{bmatrix} I_{dSi} \\ I_{qSi} \\ I_{0Si} \\ I_{mRi} \end{bmatrix} \tag{41}$$

where I_{dSi}, I_{qSi}, and I_{0Si} represent the current in the dp-axis, and $\boldsymbol{C}$ indicates the transformation matrix from the three-phase static axis to the dq-axis. The torque in the rotor part T_{Ri} is calculated using (38)–(41) as

$$T_{Ri} = K_{tR} I_{qSi} \tag{42}$$

$$K_{tR} = \frac{4\sqrt{3}}{\sqrt{2}}\Phi_{aSR} \tag{43}$$

where K_{tR} represents the torque constant. Therefore, the dynamics model of the rotor parts is described as follows:

$$T_{Ri} - T_{Mi} = J_R \frac{d\theta_{Ri}}{dt^2} \tag{44}$$

where J_R represents the inertia of the rotor parts. From (30)–(34), T_M and F_M in the static condition, where $\ddot{\theta}_{Ri} = 0$, are derived as (45) and (46), respectively,

$$T_M = T_{M1} + T_{M2} = K_{tR}\left(I_{qS1} + I_{qS2}\right) \tag{45}$$

$$F_M = F_{M1} + F_{M2} = G_r\left(-T_{M1} + T_{M2}\right)$$
$$= G_r K_{tR}\left(-I_{qS1} + I_{qS2}\right). \tag{46}$$

T_M is controlled by the sum of I_{qS1} and I_{qS2}, while F_M depends on the difference between I_{qS1} and I_{qS2}. It turns out that T_M and F_M can be controlled independently. Additionally, the proposed motor can generate a large thrust force based on G_r.

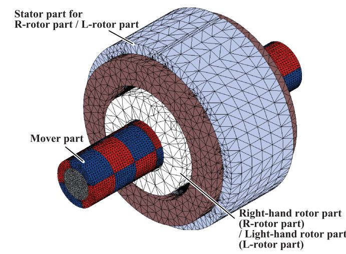

Fig. 9. Mesh model of proposed motor in finite element analysis.

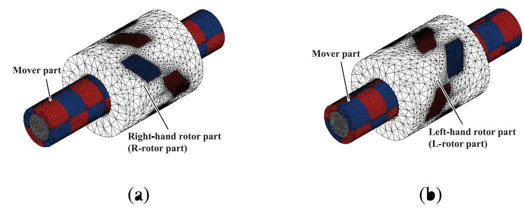

Fig. 10. Mesh models of the rotor parts. (a) R-rotor part. (b) L-rotor part.

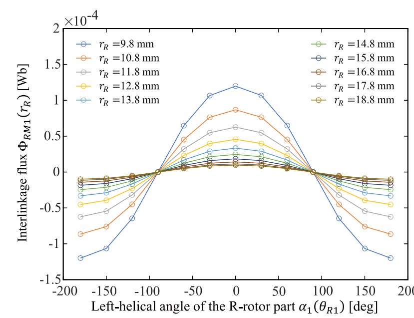

Fig. 11. Finite element analysis results of interlinkage flux interlinking with the R-rotor part.

III. Analysis of Proposed Radial-Gap Two-Degree-of-Freedom Motor

A. Analysis Environment

The proposed motor was analyzed using JMAG-Designer, which is FEA software provided by the JSOL Corporation. Figs. 9 and 10 present the 3-D analysis models, which are composed of the parameters listed in Table II. In FEA, the component of the right-hand screw was analyzed basically because the R-rotor part had the opposite structure of the L-rotor part. Therefore, the FEA analysis model was composed of the mover part, R-rotor part, and stator part for the R-rotor part.

B. Interlinkage Flux Interlinking With the R-Rotor Part and Calculation Based on the Mathematical Model

First, $\Phi_{RM1}(r_R)$ was analyzed in the condition in which $\alpha_2(\theta_{R1})$ was kept 0, and Fig. 11 presents the FEA results. $\Phi_{RM1}(r_R)$ was dependent on $\alpha_1(\theta_{R1})$ and was close to the cosine wave presented in (11). The amplitude of $\Phi_{RM1}(r_R)$ decreased as r_R increased.

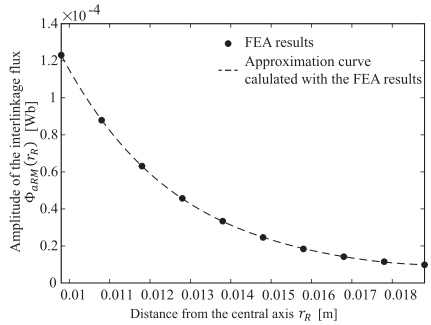

Fig. 12. Finite element analysis results of the amplitude of the interlinkage flux.

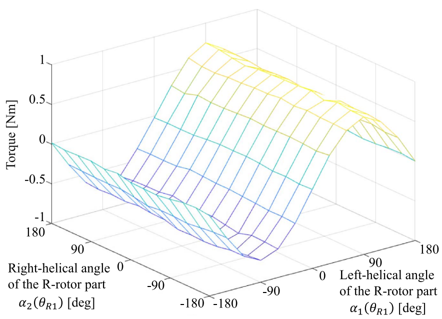

Fig. 13. Finite element analysis results of torque generated in the motor part by the R-rotor part.

Fig. 12 presents $\Phi_{aRM}(r_R)$, which is the amplitude of $\Phi_{RM1}(r_R)$. In the figure, $\Phi_{aRM}(r_R)$ is the first-order cosine component extracted from each wave in Fig. 11 by a discrete Fourier series development. The broken line represents the approximation curve calculated with Φ_{aRM} indicated by the dots in the figure. The formula of the approximation curve is as follows:

$$\Phi_{aRM}(r_R) = 18582 \cdot r_R^4 - 1262.6 \cdot r_R^3 + 32.857 \cdot r_R^2 - 0.391 \cdot r_R + 0.0018. \tag{47}$$

From the mathematical model based on (30), (32), and (47), T_{aM} and F_{aM} were calculated as (48) and (49), respectively,

$$T_{aM} = 0.7071\,\text{Nm} \tag{48}$$

$$F_{aM} = 111.1\,\text{N}. \tag{49}$$

C. Torque and Thrust Force in the Mover Part

T_{M1} and F_{M1} with different $\alpha_1(\theta_{R1})$ and $\alpha_2(\theta_{R1})$ were analyzed, and Figs. 13 and 14 present the FEA results. The results indicate that T_{M1} and F_{M1} were dependent on $\alpha_1(\theta_{R1})$ but independent of $\alpha_2(\theta_{R1})$. Additionally, T_{M1} and F_{M1} were close to sine waves depending on $\alpha_1(\theta_{R1})$.

Fig. 15 displays graphs that represent Figs. 13 and 14 two-dimensionally. In the figures, the dots indicate the average values at each $\alpha_1(\theta_{R1})$, while the broken lines indicate the approximation curves calculated with the average values. The approximation curves are composed of the first-order sine components extracted by discrete Fourier series development. The solid lines represent the calculation results based on the mathematical model. T_{aM} and F_{aM} of the calculation results are presented in (48) and (49), respectively, and the approximation curves are close to the calculation results.

Table III presents the amplitude of the approximation curves. The ratio of F_{M1} to T_{M1} is close to $G_r = 1.57 \times 10^2$ calculated by (34), and T_{M1} and F_{M1} are generated based on (30)–(34).

Additionally, T_{M2} and F_{M2} with different $\alpha_1(\theta_{R2})$ and $\alpha_2(\theta_{R2})$ were analyzed. Figs. 16 and 17 show the analysis results. T_{M2} and F_{M2} were dependent on $\alpha_2(\theta_{R2})$ but independent of $\alpha_1(\theta_{R2})$. It was confirmed that the L-rotor part had the opposite characteristics of the R-rotor part.

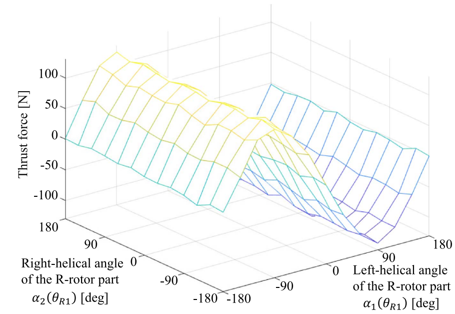

Fig. 14. Finite element analysis results of thrust force generated in the mover part by the R-rotor part.

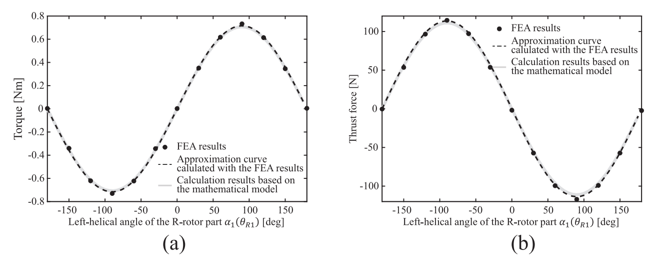

Fig. 15. Average values and approximate curves of torque and thrust force generated in the mover part by the R-rotor part. (a) Torque. (b) Thrust force.

TABLE III
COMPONENTS OF APPROXIMATION CURVES

Amplitude of T_{M1} (T_{aM}) [Nm]	Amplitude of F_{M1} (F_{aM}) [N]	$\frac{F_{aM}}{T_{aM}}$
0.7161	113.7	158.8

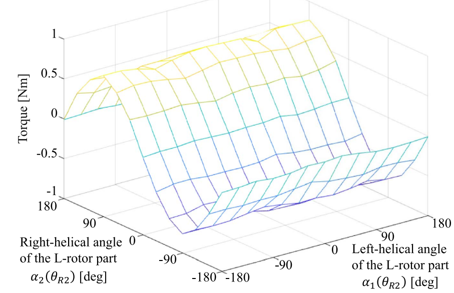

Fig. 16. Finite element analysis results of torque generated in the motor part by the L-rotor part.

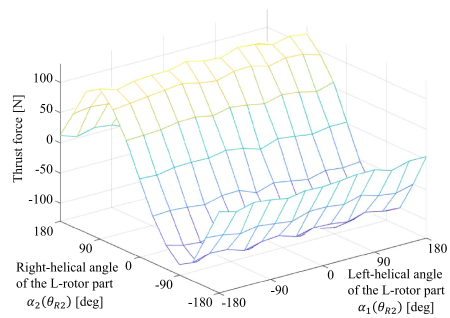

Fig. 17. Finite element analysis results of thrust force generated in the mover part by the L-rotor part.

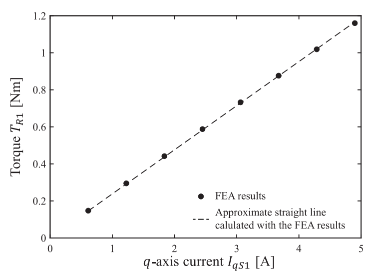

Fig. 18. Finite element analysis (FEA) results of torque generated in the R-rotor part.

D. Torque Constant

T_{R1}, which is generated by the current in the stator parts, was analyzed. Fig. 18 presents the FEA results of the torque generated in the R-rotor part. In the FEA, torque with different θ_{R1} was analyzed, while maintaining $\alpha_1(\theta_{R1}) = 0$. Therefore, FEA was performed so that torque was not generated between the R-rotor part and mover part. It included only torque generated by the current of the stator part.

In the figure, the dots indicate the FEA results at each I_{qS1}, and the broken line is an approximate straight line calculated based on the least-squares method. The formula of the approximate straight line is expressed as

$$T_{R1} = 0.2381 I_{qS1}. \tag{50}$$

Therefore, K_{tR} calculated with the FEA results is 0.2381 Nm/A.

IV. Experiments of Proposed Radial-Gap Two-Degree-of-Freedom Motor

A. Experimental Environment

Figs. 19 and 20 display the experimental machine. The machine had rotary encoders, a linear encoder, and a force sensor. The rotary encoders were E80H by AUTONICS, which were used to measure θ_{R1}, θ_{R2}, and θ_M. The linear encoder was QUANTiC by Renishaw to measure z_M, and the force sensor was PFS by Leptrino to measure T_{R1}, T_M, and F_M. The force sensor is fixed to the base plate, where the stator parts are fixed. Additionally, the mover part is connected to the force sensor mover part through the connector. The experimental parameters are presented in Table IV.

TABLE IV
EXPERIMENTAL PARAMETERS

Weight of mover part [kg]	M_M	2.53
Inertia of mover part [kgm^2]	J_M	1.05×10^{-4}
Inertia of rotor part [kgm^2]	J_R	1.95×10^{-4}
Resolution of rotary encoder [pulse/rotation]		3200
Resolution of linear encoder [m]		0.1×10^{-6}
Torque resolution of force sensor in the θ direction [Nm]		0.003
Force resolution of force sensor in the z-direction [N]		0.125

B. Torque Constant of R-Rotor Part

First, T_{R1} was measured at different I_{qS1}. In the experiment, the measurement was performed in the condition, where the mover part was detached from the experimental machine so that torque was not generated between the R-rotor part and mover part.

Fig. 21 presents the experimental results. At each I_{qS1}, T_{R1} was measured six times, and the average values are plotted as dots in the figure. The broken lines represent the approximate straight lines calculated with the measurement values. The formulas of both approximate straight lines are as follows:

$$T_{R1} = \begin{cases} 0.2222 I_{qS1} - 0.0039 & I_{qS1} > 0 \\ 0.2180 I_{qS1} + 0.0132 & I_{qS1} < 0 \end{cases}. \tag{51}$$

K_{tR} was calculated based on the average of the proportional constant in both approximate straight lines. K_{tR} calculated with the measurement values was 0.2201 Nm/A, which was close to the analysis result of $K_{tR} = 0.2381$ Nm/A.

The second term in the right side of the equation represents friction. The friction causes energy loss and changes with speed. Although the experimental system does not have the function to measure torque when rotor parts rotate, it is necessary to measure it in the future, to evaluate the energy efficiency of the proposed motor.

C. Torque and Thrust Force in the Mover Part

T_{M1} and F_{M1} were measured at different $\alpha_1(\theta_{R1})$. In the experiment, the measurement was performed in the condition where the mover part was fixed. Therefore, θ_M and z_M were kept constant. Figs. 22 and 23 present the experimental results. In the figures, the dots represent the average of the measurement values. The error bars were calculated based on standard deviation. The results indicate that T_{M1} and F_{M1} increased depending on $\alpha_1(\theta_{R1})$.

In the figures, the broken lines represent the analysis results, which are the broken lines in Fig. 15(a) and (b). The solid lines represent the calculation results, which are the solid lines in Fig. 15(a) and (b). The dots, which represent the experimental results, differed from the analysis and calculation results. The reason for the error is the difference in the magnetic flux density between the analysis model and experimental machine.

The FEA was conducted with the ideal parameter, including the residual magnetic density of the PMs. However, the actual

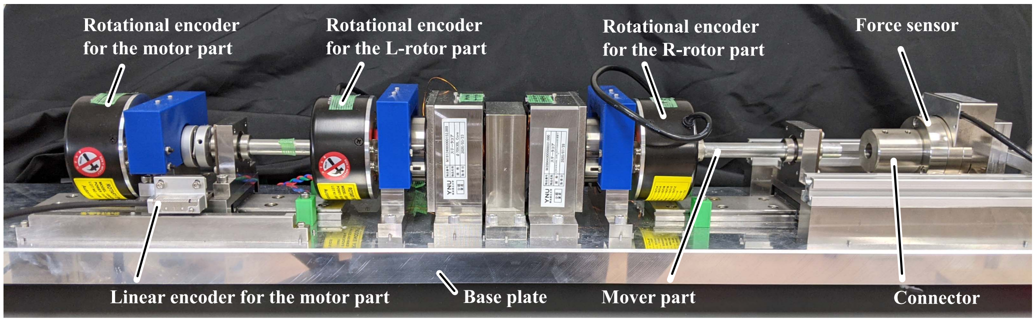

Fig. 19. Experimental machine.

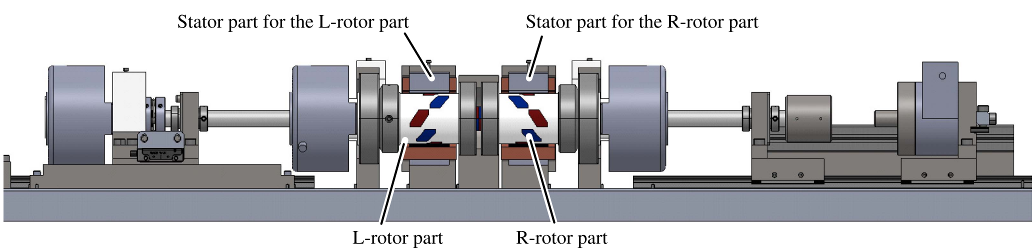

Fig. 20. Internal structure of experimental machine.

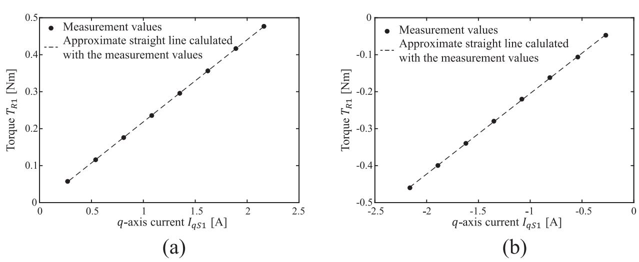

Fig. 21. Experimental results of torque in the R-rotor part generated by the current. (a) Torque generated by positive current. (b) Torque generated by negative current.

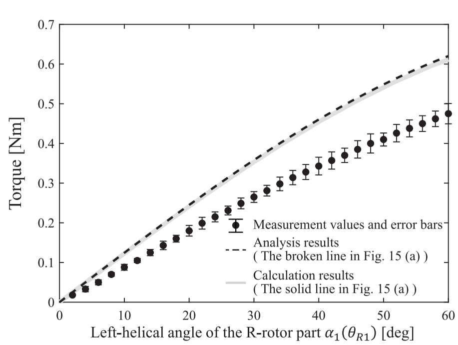

Fig. 22. Experimental results of torque in the mover part depending on $\alpha_1(\theta_{R1})$.

parameters are different from the ideal parameters because tolerance always exists in the actual machine. Table V presents the magnetic flux density of the analysis model and experimental machine. Magnetic Meter (MG-3000SD) provided by FUSO Corporation was used for the measurement. The magnetic force density on the PM's surface was measured by contacting the

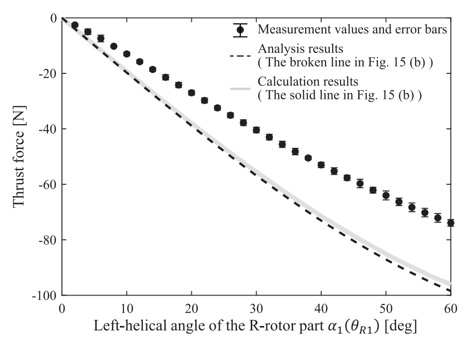

Fig. 23. Experimental results of thrust force in the mover part depending on $\alpha_1(\theta_{R1})$.

TABLE V
COMPARISON OF MAGNETIC FLUX DENSITY IN THE PERMANENT MAGNET (PM) OF THE MOVER PART

Analysis results of analysis model	Measurement results of actual PM	$\frac{B_{\mathrm{REAL}}}{B_{\mathrm{FEA}}}$
$B_{\mathrm{FEA}} = 0.394$ T	$B_{\mathrm{REAL}} = 0.301$ T	76%

sensing point to the surface. It was analyzed and measured at the center point of the surface of the PM, which was composed of the mover part. Fig. 24 presents the analysis point and measurement point. Table V indicates that the PM of the experimental machine had a lower magnetic flux density than the analysis results. The ratio of the measurement results to the analysis results is 76%.

The thrust force and torque are proportional to the residual magnetic density, as (31) and (33). In Figs. 25 and 26, the broken lines indicate the FEA results compensated with the ratio of the magnetic density. The gray lines are the calculation

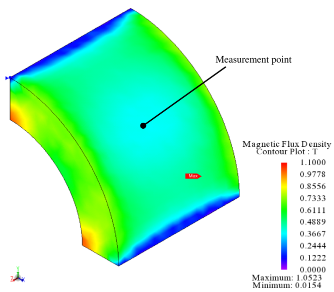

Fig. 24. Measurement point for magnetic flux density in the permanent magnet of the mover part.

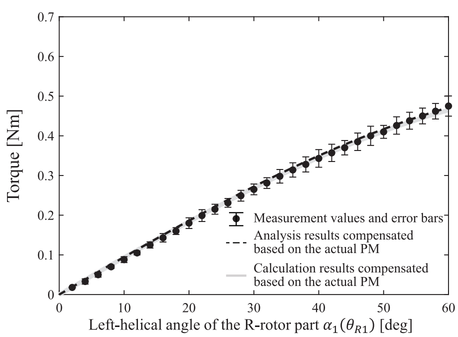

Fig. 25. Experimental results of torque and a comparison with the analysis and calculation results compensated based on Table V.

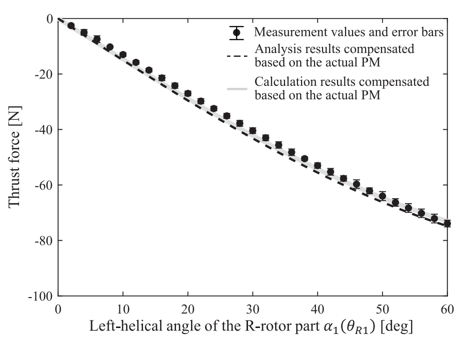

Fig. 26. Experimental results of thrust force and a comparison with analysis and calculation results compensated based on Table V.

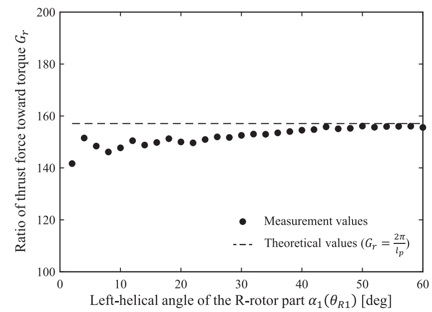

Fig. 27. G_r calculated with measurement values presented in Fig. 25 and 26.

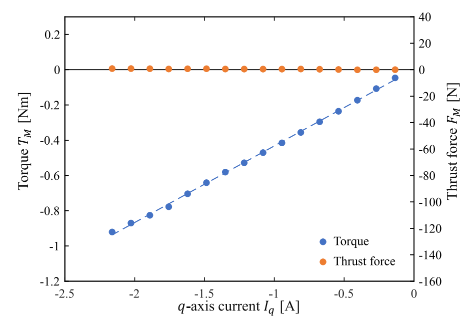

Fig. 28. Experimental results of T_M and F_M generated by I_{qS1} and I_{qS2} in Case 1.

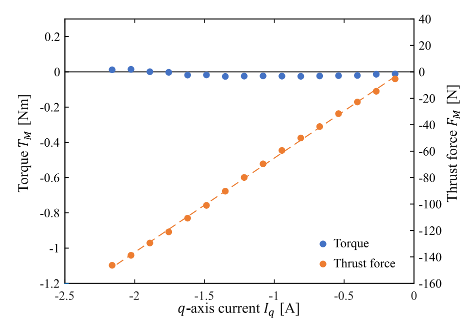

Fig. 29. Experimental results of T_M and F_M generated by I_{qS1} and I_{qS2} in Case 2.

results compensated with the ratio of the magnetic density. They indicate T_{M1} and F_{M1} calculated based on $T_{aM} \times 76\%$, $F_{aM} \times 76\%$, (30), and (32). The dots represent the same data as the measurement values in Figs. 22 and 23. The measurement values are close to these lines, thereby confirming the effectiveness of (30) and (32).

Figs. 27 presents the ratio of the thrust force to the torque. In the figure, the dots indicate G_r calculated with the measurement values presented in Figs. 25 and 26. The broken line represents $G_r = \frac{2\pi}{l_p}$. As $\alpha_1(\theta_{R1})$ decreased, the difference between the experimental results and $\frac{2\pi}{l_p}$ increased. The reason for this may be friction. As $\alpha_1(\theta_{R1})$ decreased, the ratio of friction to F_{M1} increased. Therefore, G_r was small when $\alpha_1(\theta_{R1})$ was small. In contrast, the experimental result approached $G_r = \frac{2\pi}{l_p}$ as $\alpha_1(\theta_{R1})$ increased.

D. Torque and Thrust Force Generated by Current in Two Stator Parts

In the experiment, the current was input to both stator parts to investigate the independent generation of T_M and F_M. Two experimental cases were examined: Case 1 and Case 2. In each case, the current input to both stator parts was defined as follows:

$$\text{Case1} \quad I_q = I_{qS1} = I_{qS2} \tag{52}$$

$$\text{Case2} \quad I_q = -I_{qS1} = I_{qS2}. \tag{53}$$

Figs. 28 and 29 present the experimental results. In Case 1, T_M increased depending on the increase of I_q. In Case 2, F_M increased depending on the increase of I_q. In contrast, the generation of F_M in Case 1 and of T_M in Case 2 was suppressed. The results indicate that T_M was generated by the sum of I_{qS1} and I_{qS2}, while F_M was generated by the difference between I_{qS1} and I_{qS2}. Therefore, T_M and F_M were generated independently.

In the figures, broken lines indicate the approximate straight lines of T_M in Case 1 and F_M in Case 2. The formulas of both approximate straight lines are as follows:

$$T_M = 0.2173\,(I_{qS1} + I_{qS2}) \tag{54}$$

$$F_M = G_r \times 0.2173\,(-I_{qS1} + I_{qS2}) \tag{55}$$

$$G_r = 164.0. \tag{56}$$

The error between (56) and $G_r = \frac{2\pi}{l_p}$ was less than 4%. The results thus confirm the effectiveness of (45) and (46).

V. Conclusion

This article proposes a radial-gap 2-DOF motor based on a magnetic screw structure. The motor generates a torque and thrust force simultaneously and independently. Additionally, the motor can generate a large thrust force due to the magnetic screw structure. In this article, the structure of the proposed motor and mathematical modeling are described, and the analysis and experimental results demonstrate the effectiveness of the mathematical modeling.

The proposed motor can contribute to the minimization of multi-DOF systems, such as industrial robots, because it has two DOFs. Furthermore, it can offer lower energy loss than a ball screw, in which a nut and screw are coupled with physical contact, because the rotor parts and mover part are coupled by means of magnetic force.

In future work, it is necessary to measure the energy loss of the proposed motor. In addition, the proposed motor has rotor parts and stator parts and is thus composed of a multimass model. It is necessary to design a controller based on the multimass model to control the proposed motor.

Additionally, the proposed motor potentially has both of different driving systems for the rotor parts. The usefulness of the combination of different driving systems has been indicated by the hybrid actuator system [23]. The hybrid actuator system for the proposed motor is worth considering.

References

[1] W. Wang, J. Wang, G. W. Jewell, and D. Howe, "Design and control of a novel spherical permanent magnet actuator with three degrees of freedom," *IEEE/ASME Trans. Mechatronics*, vol. 8, no. 4, pp. 457–468, Dec. 2003.

[2] B. Li, G. D. Li, and H. F. Li, "Magnetic field analysis of 3-DOF permanent magnetic spherical motor using magnetic equivalent circuit method," *IEEE Trans. Magn.*, vol. 47, no. 8, pp. 2127–2133, Aug. 2011.

[3] J. F. P. Fernandes and P. J. C. Branco, "The shell-like spherical induction motor for low-speed traction: Electromagnetic design, analysis, and experimental tests," *IEEE Trans. Ind. Electron.*, vol. 63, no. 7, pp. 4325–4335, Jul. 2016.

[4] G. Krebs, A. Tounzi, B. Pauwels, D. Willemot, and F. Piriou, "Modeling of a linear and rotary permanent magnet actuator," *IEEE Trans. Magn.*, vol. 44, no. 11, pp. 4357–4360, Nov. 2008.

[5] T. T. Overboom, J. W. Jansen, E. A. Lomonova, and F. J. F. Tacken, "Design and optimization of a rotary actuator for a two-degree-of-freedom $z\phi$-Module," *IEEE Trans. Ind. Appl.*, vol. 46, no. 6, pp. 2401–2409, Nov./Dec. 2010.

[6] J. Si, H. Feng, L. Ai, Y. Hu, and W. Cao, "Design and analysis of a 2-DOF split-stator induction motor," *IEEE Trans. Energy Convers.*, vol. 30, no. 3, pp. 1200–1208, Sep. 2015.

[7] L. Xie, J. Si, Y. Hu, and H. Feng, "Helical motion analysis of the 2-degree-of-freedom split-stator induction motor," *IEEE Trans. Magn.*, vol. 55, no. 6, Jun. 2019, Art. no. 8103705.

[8] L. Xu, M. Lin, X. Fu, and N. Li, "Analysis of a double stator linear rotary permanent magnet motor with orthogonally arrayed permanent magnets," *IEEE Trans. Magn.*, vol. 52, no. 7, Jul. 2016, Art. no. 8203104.

[9] S. Tanaka, T. Shimono, and Y. Fujimoto, "Development of a cross-coupled 2DOF direct drive motor," in *Proc. IEEE Int. Conf. Ind. Electron.*, 2014, pp. 508–513.

[10] Y. Hatta and T. Shimono, "Analysis and experimental verification of cross-coupled 2-DOF SPM motor with halbach array," *IEEJ J. Ind. Appl.*, vol. 9, no. 2, pp. 177–190, Mar. 2020.

[11] T. Shimono, S. Tanaka, Y. Hatta, H. Asai, and Y. Fujimoto, "Mathematical modeling, finite element analysis, and experimental verification of cross-coupled 2-DOF tubular SPMSM," in *Proc. IEEJ Int. Workshop Sensing, Actuation, Motion Control, Optim.*, 2021, pp. 138–143.

[12] D. S. Raghunvanshi, S. I. Moore, A. J. Fleming, and Y. K. Yong, "Electrode configurations for piezoelectric tube actuators with improved scan range and reduced cross-coupling," *IEEE/ASME Trans. Mechatronics*, vol. 25, no. 3, pp. 1479–1486, Jun. 2020.

[13] Y. Tian *et al.*, "A spatial deployable three-DOF compliant nano-positioner with a three-stage motion amplification mechanism," *IEEE/ASME Trans. Mechatronics*, vol. 25, no. 3, pp. 1322–1334, Jun. 2020.

[14] J. Zhang, W. J. Zhang, J. Hesselbach, and H. Kerle, "Development of a two-degree-of-freedom piezoelectric rotary-linear actuator with high driving force and unlimited linear movement," *Rev. Sci. Instrum.*, vol. 77, no. 3, 2006, Art. no. 035112.

[15] K. Tsurumoto and S. Kikuchi, "A new magnetic gear using permanent magnet," *IEEE Trans. Magn.*, vol. 23, no. 5, pp. 3622–3624, Sep. 1987.

[16] K. Atallah and D. Howe, "A novel high-performance magnetic gear," *IEEE Trans. Magn.*, vol. 37, no. 4, pp. 2844–2846, Jul. 2001.

[17] X. Zhu, Z. Xiang, L. Quan, Y. Chen, and L. Mo, "Multimode optimization research on a multiport magnetic planetary gear permanent magnet machine for hybrid electric vehicles," *IEEE Trans. Ind. Electron.*, vol. 65, no. 11, pp. 9035–9046, Nov. 2018.

[18] P. O. Rasmussen, T. O. Andersen, F. T. Jorgensen, and O. Nielsen, "Development of a high-performance magnetic gear," *IEEE Trans. Ind. Appl.*, vol. 41, no. 3, pp. 764–770, May/Jun. 2005.

[19] S. Pakdelian, N. W. Frank, and H. A. Toliyat, "Principles of the trans-rotary magnetic gear," *IEEE Trans. Magn.*, vol. 49, no. 2, pp. 883–889, Feb. 2013.

[20] J. Wang, K. Atallah, and W. Wang, "Analysis of a magnetic screw for high force density linear electromagnetic actuators," *IEEE Trans. Magn.*, vol. 47, no. 10. pp. 4477–4480, Oct. 2011.

[21] C. S. Christophe and Y. Fujimoto, "Enactment-based direct-drive test of a novel radial-gap helical RotLin machine," *IEEE Trans. Ind. Appl.*, vol. 54, no. 2, pp. 1273–1282, Mar./Apr. 2018.

[22] Y. Hatta, Y. Fujimoto, and T. Shimno, "Investigation into radial-gap two-degree-of-freedom motor based on a magnetic screw structure," *IEEJ Tech. Meeting "Transportation and Electric Railway" and "Linear Drive" IEE Jpn./Transp. Electric Railway Study Group*, 2020, pp. 47–52.

[23] P. Ouyang, Q. Li, W. Zhang, and L. Guo, "Design, modeling and control of a hybrid machine system," *Mechatronics*, vol. 14, no. 10, pp. 1197–1217, Dec. 2004.

Yoshiyuki Hatta (Member, IEEE) received the B.E., M.E., and Ph.D. degrees in electrical and computer engineering from Yokohama National University, Yokohama, Japan, in 2010, 2012, and 2020, respectively.

From 2012 to 2015, He was with Honda Motor Company, Ltd., Tokyo, Japan. From 2015 to 2017, he was with Chikashima International Patent Firm, Japan. He is currently a Specially Appointed Assistant Professor with Intelligent Production Technology Research & Development Center For Aerospace, Gifu University, Gifu, Japan. His research interests include electrical actuators, motion control, robotics, and haptics.

Yasutaka Fujimoto (Senior Member, IEEE) was born in Kanagawa, Japan. He received the B.E., M.E., and Ph.D. degrees in electrical and computer engineering from Yokohama National University, Yokohama, Japan, in 1993, 1995, and 1998, respectively.

In 1998, he was with the Department of Electrical Engineering, Keio University, Yokohama, Japan. Since 1999, he has been with the Department of Electrical and Computer Engineering, Yokohama National University, where he is currently a Professor. His research interests include actuators, robotics, manufacturing automation, and motion control.

Dr. Fujimoto is a Senior Member of IEE of Japan and a member of Robotics Society of Japan. He was the recipient of the IEEE/ASME Transactions on Mechatronics Best Paper Award in 2020. He is an Associate Editor for IEEE TRANSACTIONS ON INDUSTRIAL ELECTRONICS and a Vice Chief for the *IEEJ Journal of Industry Applications*.

Tomoyuki Shimono (Senior Member, IEEE) received the B.E. degree in mechanical engineering from Waseda University, Tokyo, Japan, in 2004, and the M.E. and Ph.D. degrees in integrated design engineering from Keio University, Yokohama, Japan, in 2006 and 2007, respectively.

He is currently an Associate Professor with the Faculty of Engineering, Yokohama National University, Yokohama, Japan. His research interests include haptics, motion control, medical and rehabilitation robots, and actuators.

Kazuaki Ito (Senior Member, IEEE) received the B.S., M.S. and Ph.D. degrees in electrical and computer engineering from the Nagoya Institute of Technology, Nagoya, Japan, in 1998, 2000, and 2003, respectively.

In 2003, he joined the Department of Electrical and Electronic Engineering, National Institute of Technology, Toyota College, Toyota, Japan, as a Research Associate, where he became an Associate Professor, in 2009. From 2012 to 2013, he was a Visiting Scholar with the Department of Management and Engineering, University of Padova, Vicenza, Italy. He moved to the Department of Mechanical Engineering, Gifu University, Gifu, Japan, as an Associate Professor, in 2017. He has been a Professor, since 2022. His research interests include applications of motion control theory and soft computing techniques for mechatronic systems and real-world haptics.

Dr. Ito is a Senior Member of the Institute of Electrical Engineers of Japan, and a Member of the Japan Society for Precision Engineering, the Society of Instrument and Control Engineers, and the Japan Society of Mechanical Engineers. He is a Technical Editor for the IEEE/ASME TRANSACTIONS ON MECHATRONICS.